ADVANCED HEALTHCARE MATERIALS
www.advhealthmat.de

Effects of Polymer 3D Architecture, Size, and Chemistry on Biological Transport and Drug Delivery In Vitro and in Orthotopic Triple Negative Breast Cancer Models

Amanda K. Pearce, Akosua B. Anane-Adjei, Robert J. Cavanagh, Patricia F. Monteiro, Thomas M. Bennett, Vincenzo Taresco, Phil A. Clarke, Alison A. Ritchie, Morgan R. Alexander, Anna M. Grabowska, and Cameron Alexander**

The size, shape, and underlying chemistries of drug delivery particles are key parameters which govern their ultimate performance in vivo. Responsive particles are desirable for triggered drug delivery, achievable through architecture change and biodegradation to control in vivo fate. Here, polymeric materials are synthesized with linear, hyperbranched, star, and micellar-like architectures based on 2-hydroxypropyl methacrylamide (HPMA), and the effects of 3D architecture and redox-responsive biodegradation on biological transport are investigated. Variations in "stealth" behavior between the materials are quantified in vitro and in vivo, whereby reduction-responsive hyperbranched polymers most successfully avoid accumulation within the liver, and none of the materials target the spleen or lungs. Functionalization of selected architectures with doxorubicin (DOX) demonstrates enhanced efficacy over the free drug in 2D and 3D in vitro models, and enhanced efficacy in vivo in a highly aggressive orthotopic breast cancer model when dosed over schedules accounting for the biodistribution of the carriers. These data show it is possible to direct materials of the same chemistries into different cellular and physiological regions via modulation of their 3D architectures, and thus the work overall provides valuable new insight into how nanoparticle architecture and programmed degradation can be tailored to elicit specific biological responses for drug delivery.

1. Introduction

For disease targets such as cancer, polymeric nanocarriers have been shown to be effective for achieving site-specific drug delivery while minimizing off-target toxicity.[1–3] Typically, small molecule chemotherapy drugs have poor in vivo properties, such as a short blood half-life, rapid clearance through metabolism, degradation or activation of an immune response, and poor accumulation in cells due to poor blood flow and drug efflux pumps.[4] The use of polymers as drug carriers aims to overcome these drawbacks through achieving longer circulation times, enhanced uptake in disease sites and increased specificity of delivery.[5–7] However, in order to obtain selective tumor uptake of nanoparticle drug carriers, the delivery systems must meet several criteria, such as an appropriate size range for diffusion out of the vasculature, prolonged circulation time in the bloodstream to allow for efficient uptake, reduced clearance from the bloodstream by avoidance of recognition by macrophages, and stability of the carrier during circulation.[8,9] Previous literature suggests that while larger nanocarriers have prolonged circulation times in the blood, particles over ≈100 nm suffer from poor tumor penetration, particularly in the case of poorly vascularized and necrotic/hypoxic tumors.[10] Conversely, particles of a size range less than 30 nm possess good tumor penetration properties, however the blood circulation times are often decreased due to the smaller size.[11,12] In addition, it has been observed that nanoparticle properties such as chemistry, size, shape, and

Dr. A. K. Pearce
School of Chemistry
University of Birmingham
Edgbaston B15 2TT, UK
E-mail: a.k.pearce@bham.ac.uk

Dr. A. K. Pearce, Dr. A. B. Anane-Adjei, Dr. R. J. Cavanagh, Dr. P. F. Monteiro, Dr. V. Taresco, Prof. M. R. Alexander, Prof. C. Alexander
School of Pharmacy
University of Nottingham
Nottingham NG72RD, UK
E-mail: Cameron.Alexander@nottingham.ac.uk

Dr. T. M. Bennett
School of Chemistry
University of Nottingham
Nottingham NG72RD, UK

Dr. P. A. Clarke, A. A. Ritchie, Prof. A. M. Grabowska
School of Medicine
University of Nottingham
Nottingham NG72RD, UK

The ORCID identification number(s) for the author(s) of this article can be found under https://doi.org/10.1002/adhm.202000892

DOI: 10.1002/adhm.202000892

aspect ratio all have an effect on pharmacokinetics, tumor penetration and organ accumulation.[13–17] These concepts have been reviewed in recent years due to the importance of achieving the appropriate trade-off between nanoparticle characteristics to achieve both prolonged circulation and good penetration into a solid tumor mass.[18–20] However, while there have been investigations of many nanoparticle sizes and shapes, there remain questions relating to how nanoparticles of specific sizes and architectures, but retaining the same surface chemistry behave in in vivo environments.

The surface chemistry presented by nanoparticle drug delivery systems to the local biological environment is known to be of crucial importance for achieving prolonged circulation within the bloodstream.[21] Typically, polyethylene glycol (PEG)-based polymers are utilized for their well-documented stealth properties in vivo to prevent the nonspecific adsorption of serum proteins and shield from receptor mediated uptake by the reticuloendothelial system (RES).[22,23] However, it has also been observed that there are antibodies produced in the body that recognize PEGylated materials (anti-PEG Abs) resulting in a reduced treatment efficacy, as well as an increased risk of adverse side effects to the materials after administration.[24] As a result, a variety of alternative synthetic polymers have been investigated as coatings or shell materials for drug delivery nanoparticles, such as poly(amino acid)s,[25,26] poly(2-oxazoline)s,[27,28] poly(glycerol),[29,30] and poly(*N*-(2-hydroxypropyl)methacrylamide) (pHPMA).[31,32] The potential of poly(*N*-(2-hydroxypropyl)methacrylamide) for biological applications was first highlighted by Kopeček et al. in the 1970s.[33,34] Since then, examples of pHPMA–drug conjugates have been widespread in the literature including reports of use in clinical trials[35–38] and these continue to show promise in the field.[39–41]

Particular disease sites present inherent abnormalities; in tumor tissues these include low pH, hypoxia, high temperature, over-expressed proteins and enzymes and elevated levels of reactive small molecules such as metabolites and reactive oxygen species (ROS), which provide opportunities for site-specific delivery of therapeutics, as well as stimuli for controlled degradation of the nanocarriers.[42–44] Particularly, the higher concentrations of glutathione (GSH) found in the microenvironment of certain tumor types, and especially those of certain breast cancers, can be exploited through the inclusion of disulfide bonds within a polymeric system.[43,45,46] Following accumulation of a nanoparticle carrier within a tumor site, the enhanced local GSH concentration can promote polymer breakdown through cleavage of the disulfide bonds.[47,48] Another commonly exploited stimulus for tumor-targeted delivery is the localized acidic environment of tumors, with pH ranges of ≈4.5–6.5, providing opportunity for triggered release through acid-labile linkages.[49–54]

In this work, the effects of differing hydrodynamic size, physical conformations and programmed biodegradation of drug delivery nanomaterials formulated from HPMA is investigated, with reference to the internalization of the materials in cell lines, in transit in the body, and in a selected subset, the antitumor efficacy in a relevant aggressive orthotopic triple negative breast cancer (TNBC) model. While polymeric HPMA materials have been previously studied as drug delivery carriers, the majority of materials have been synthesized through free-radical polymerizations.[55,56] More recently, pHPMAs have been synthesized through controlled radical polymerization techniques, namely, reversible addition fragmentation chain transfer (RAFT) polymerization, giving greater control over the molecular weights of the resultant materials, and providing access to more versatility in the final structures that can be produced.[39,57–60] Based on the potential of pHPMA-based polymeric drug delivery polymers, we aimed to exploit the range of architectures and monomer compatibility provided by RAFT polymerization to thoroughly investigate if materials of the same chemistries can be directed into different cellular and physiological regions via modulation of their 3D architectures and size, thus providing crucial new insight into tailoring of nanomaterials to elicit specific biological responses for drug delivery.

To achieve this, four target polymer architectures were synthesized by RAFT polymerization to produce materials with the same underlying chemistries, in order to isolate the effects of the physical variations. Hyperbranched polymers were chosen as the initial architecture of materials to investigate based on their known potential for tumor targeting and uptake in vivo.[61,62] Further to this, larger architectures were proposed, namely star, high molecular weight linear and core-crosslinked micellar polymers. A combination of nondegradable hyperbranched and redox-responsive architectures were synthesized through parallel synthetic routes in order to access a wide size range of materials from 5 to 60 nm with multiple stimuli-responsive mechanisms of degradation, depicted in **Scheme 1**. The resultant materials were screened in vitro for their stability, degradation in reducing environments, cytocompatibility and uptake by macrophages, and for their organ distribution in vivo. As a result of the screening process, two lead nanoparticles were selected for further functionalization with a model anticancer drug doxorubicin via hydrazone-linker conjugation on the nanoparticles. The potency of the polymer prodrug in comparison to free drug was evaluated in vitro in monolayer and 3D spheroid cultures and in vivo in an orthotopic model of triple negative breast cancer. When the dosing regime was adjusted to account for the varying distribution kinetics, enhanced efficacy in terms of reductions in tumor volume were demonstrated compared to free DOX, highlighting both the role of polymer structure in modulating biodistribution and the potential of these delivery systems for breast cancer therapy.

2. Results and Discussion

2.1. Synthesis of pHPMA in Different Architectures

Synthetic routes were developed that allowed production of a set of pHPMA materials from a small set of four starting monomers and two chain transfer agents, using an aqueous RAFT polymerization strategy to allow construction of the target architectures through minimal variations of the synthetic conditions (Scheme 1). In this way, the influence of the physical factors could be investigated while maintaining the same particle chemistry presented by the polymers in biological environments. In particular, the proposed synthetic routes and architectures were designed to lead to unimolecular or core-crosslinked nanoparticles, giving the possibility to investigate a range of surface topologies, chemical group density, ability to conjugate drugs and a wide accessible particle size range of interest for drug delivery applications, while still maintaining a high stability in solution

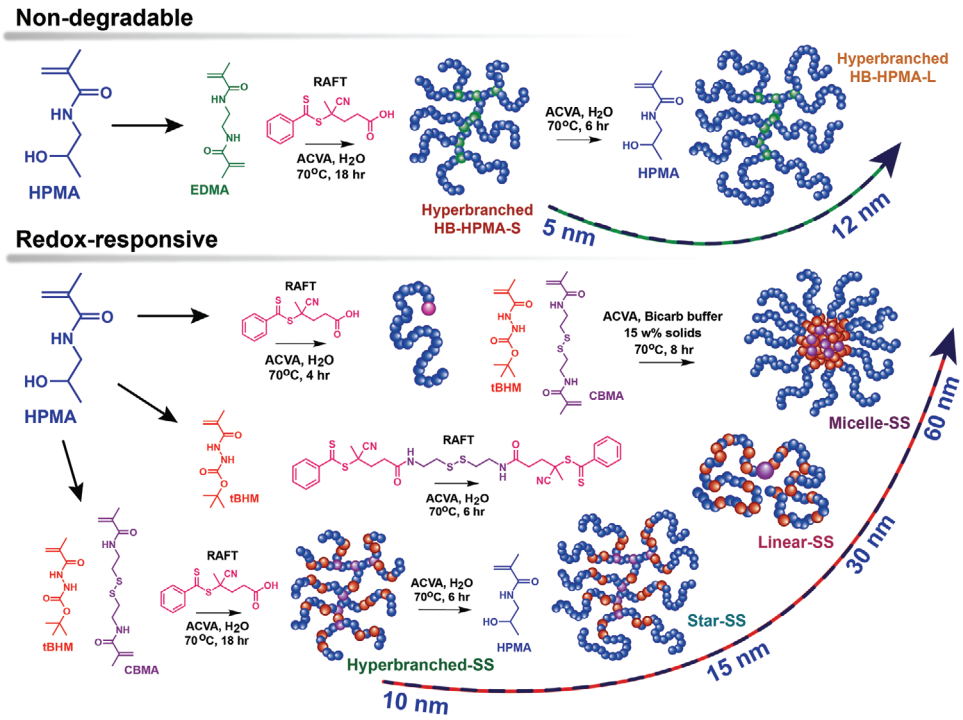

Scheme 1. Parallel synthetic routes were developed using reversible addition fragmentation chain transfer polymerization (RAFT) of HPMA for the synthesis of materials with both varying architectures and increasing physical sizes. Hyperbranched through to micelle structures resulted in particles of a size range 5–60 nm, maintaining the same surface chemistries. Materials featuring disulfide bonds are indicated by SS in the nomenclature.

and thus clinical applicability. Two classes of materials were synthesized: nondegradable pHPMAs in hyperbranched architectures as control materials, as well as redox-responsive architectures featuring disulfide bridges (SS), allowing disassembly of the polymer architectures in the intracellular milieu of breast cancer cells which overexpress GSH. A central disulfide bridge was conferred upon the redox-responsive materials through the design of cystamine bismethacrylamide (CBMA) and a degradable bis-RAFT agent (4-cyanopentanoic acid)-4-dithiobenzoate-SS-4-cyanopentanoic acid)-4-dithiobenzoate, CADB-SS-CADB), which facilitated the synthesis of varying 3D nanomaterials with degradable regions as the focal point of each architecture. This ensured biodegradability through disassembly of the parent polymer structure to produce smaller intact linear fragments of the pHPMA backbone, and thus predictable breakdown products and profiles. The further incorporation of a *t*-butoxycarbonyl (boc)-protected hydrazide methacrylate (*t*BHM) into the redox-responsive architectures provided both a degree of hydrophobicity and the capability for covalent attachment of chemotherapeutics.

Each final polymer had a minimum monomer ratio of 80 mol/mol% HPMA, in order to ensure overall water solubility of the materials,[63] as well as stealth properties in vivo, and up to 20 mol/mol% of the *t*BHM units. Hyperbranched polymers (HBs) were synthesized as previously described,[63] initially employing a nondegradable bifunctional ethylene methacrylamide (EDMA) as the crosslinking unit, resulting in small, unimolecular globular particles (hyperbranched small; HB-HPMA-S). The branched core was also further chain extended with additional HPMA to yield larger particles (hyperbranched large; HB-HPMA-L). To confer redox-responsiveness to the same architecture, the synthesis was repeated employing CBMA as the crosslinking unit, resulting in HBs with a high degree of redox-reducible branching points with a 5 mol% (hyperbranched-SS low hydrophobic; HB-SS-LH) and 20 mol% incorporation of *t*BHM (hyperbranched-SS high hydrophobic; HB-SS-HH).

Star-type architectures were achieved through chain extension of the HB-SS-HH with additional HPMA at a low (50) and a high (100) target degree of polymerization (DP), resulting in slightly larger unimolecular particles (Star-SS small, Star-SS-S; Star-SS large, Star-SS-L) with a nondegradable HPMA corona. A high molecular weight linear polymer was synthesized as a random copolymer of HPMA and *t*BHM at an 80:20 mol/mol ratio, utilizing CADB-SS-CADB to provide a central disulfide bridge in the polymer main chain (Linear-SS). Finally, core-crosslinked micelles of AB block copolymers were achieved by utilizing a polymerization-induced self-assembly (PISA) process. First, an HPMA macroRAFT agent was synthesized, followed by chain extension with *t*BHM to form the block polymer in water, driving self-assembly of the polymers into micelles as the DP of the *t*BHM block increased. Crosslinking was achieved in situ through inclusion of CBMA during the second polymerization step to form micelles stabilized by disulfide links (Micelle-SS). The synthetic schemes toward the final pHPMA materials are depicted in Scheme 1.

2.2. Physical Characterization of pHPMAs

The absolute molecular weight of each polymer (without reference to linear standards) was measured through aqueous size

A

	Mn (SEC-MALLS)	$Đ_M$	SS per polymer (mol%)	D_h (DLS)	PDI	Zeta Potential (mV)
HB-HPMA-S	15 kDa	1.4	0	5.5 nm	0.125	-20.5
HB-HPMA-L	22 kDa	1.9	0	12 nm	0.163	-11.5
HB-SS-LH	50 kDa	1.3	10	8 nm	0.136	-18.9
HB-SS-HH	58 kDa	1.5	10	10 nm	0.141	-24.1
Star-SS-S	86 kDa	1.9	7	12 nm	0.146	-16.6
Star-SS-L	122 kDa	1.6	5	15 nm	0.151	-15.3
Linear-SS	257 kDa	1.4	1	30 nm	0.195	-5.47
Micelle-SS	3,000 kDa	1.3	5	60 nm	0.086	-20.8

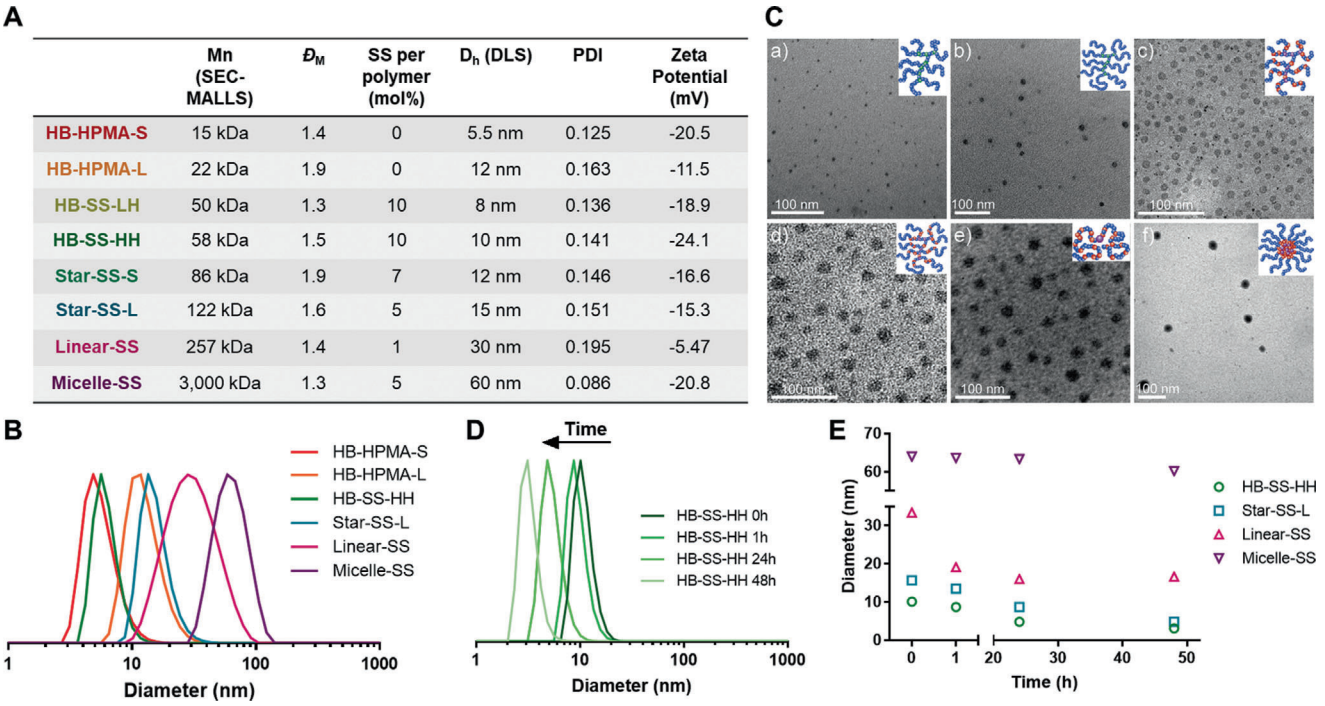

Figure 1. A) Physical characterization of varying architecture pHPMAs. B) Dynamic light scattering measurements. C) Transmission electron microscopy images of a) HB-HPMA-S, b) HB-HPMA-L, c) HB-SS-HH, d) Star-SS-L, e) Linear-SS, and f) Micelle-SS (scale bar: 100 nm). D) Degradation studies of redox-responsive pHPMAs showing shifts in DLS traces for the HB-SS-HH over time and E) change in diameter of all architectures over time in 10×10^{-3} M GSH after incubation at 37 °C.

exclusion chromatography - multi-angle laser light scattering (SEC-MALLS) (dn/dc = 0.158) (**Figure 1**A). Due to the complex nature of the polymer architectures synthesized in this work, molecular weight analysis through SEC-MALLS was most representative of the absolute molecular weight, rather than Mn calculated through proton nuclear magnetic resonance spectroscopy(^{1}H NMR) (Figures S1 and S2, Supporting Information). The nondegradable hyperbranched polymers, HB-HPMA-S and HB-HPMA-L, had the smallest molecular weights of 15 and 22 kDa, respectively. By utilizing the disulfide crosslinker, CMBA, as well as a higher mol ratio of crosslinker and RAFT agent to HPMA, a larger overall molecular weight could be achieved for the HB-SS-LH and HB-SS-HH, of 50 and 58 kDa, respectively. Following chain extension of the HB-SS-HH with additional HPMA, larger star architectures, Star-SS-S and Star-SS-L, of molecular weights 86 and 122 kDa were reached. The absolute molecular weight of the linear polymer, Linear-SS, was 257 kDa. Finally, the core-crosslinked micelles, Micelle-SS, synthesized through dispersion polymerization showed a single self-assembled species by SEC, with molecular weight quantification of 3,000 kDa.

All materials were sized using dynamic light scattering (DLS), confirming all polymers were present in solution (phosphate buffered saline, PBS) as a monodisperse population with a range of hydrodynamic diameters from 5 nm for the nondegradable HBs up to 60 nm for the core-crosslinked micelles (Figure 1B). To corroborate the presence of a single nanoparticle population from the DLS analysis, all polymers were also imaged using transmission electron microscopy (TEM), which confirmed that all polymer architectures were discrete and uniform globular entities (Figure 1C). It could thus be concluded that in addition to achieving different polymer architectures, a range of physical sizes and polymer molecular weights were also produced, allowing investigation into the biological effects of these variations while maintaining the same particle chemistry throughout.

Based on the physical characterization, it was evident that Linear-SS self-assembled in water, as DLS and TEM both confirmed the formation of particulate species of ≈30 nm diameter. It was hypothesized that the random amphiphilic copolymer was assembling into flower-like micelle structures as previously described due to the presence of the *t*BHM units.[64–66] To evaluate this, critical micelle/aggregation concentration (CMC/CAC) measurements were performed using a DLS-based CMC/CAC method, and the results are shown in Figure S3 (Supporting Information). It could be observed that the linear polymer indeed exhibited a CMC at ≈4 µg mL^{-1}, thus confirming the ability for this material to self-assemble. Unexpectedly, a CMC could also be observed for the star polymers and the core-crosslinked micelles, at 9 and 12 µg mL^{-1} respectively,[67] but was not observed for the hyperbranched polymers. As well as the linear polymers, the star materials can also be considered to be random copolymers with both hydrophobic and hydrophilic regions, and so it is likely that self-assembly can occur in the same way due to association of the hydrophobic segments as previously described.[67,68]

2.3. In Vitro Stability and Controlled Degradation of pHPMAs

The surface charge, or zeta potential, of a polymeric nanoparticle is known to influence its behavior in biological environments,

both in terms of stability of the polymer suspension as well as interactions with proteins in the body.[69,70] A slightly negative zeta potential (from neutral to −25 mV) should confer polymeric nanoparticles with resistance to aggregation and reduced interactions with proteins.[71] Zeta potentials determined for all pHPMA materials confirmed a negative surface charge, in accordance with previous literature on pHPMAs. It is interesting to note that the zeta potential of the linear polymer was closer to neutral than for the core-crosslinked micelles, despite both architectures being self-assembled nanoparticles. We suggest that the PISA-produced micelles exhibited a denser pHPMA corona, resulting in the more negative surface charge, in comparison to a looser flower-micelle self-assembled structure from the linear random copolymer.[72]

The stability of the pHPMAs to aggregation or disassembly under biologically relevant conditions was assessed using a range of DLS-based assays, due to the fast response time and ease of detection of aggregation within each sample. For all experiments, the value of the laser attenuation was kept constant, and thus any significant changes in stability or aggregation would result in a change in the DLS peak intensity. First, stability in cell culture conditions was tested by incubating each material in Dulbecco's Modified Eagle Medium (DMEM) at 37 °C, and measuring by DLS over time. It can be seen in Figure S4 (Supporting Information) that all materials were stable for the duration of the experiment, with no significant changes in the DLS traces observed.

The degradation of the redox-responsive pHPMAs through disulfide cleavage was investigated through DLS using 10×10^{-3} M glutathione (GSH) to mimic the intracellular concentrations within TNBC cells.[73] Each material was incubated in GSH in PBS at 37 °C and measured at 1, 24, and 48 h to assess any changes in size.[74] The linear, star and hyperbranched structures showed a decrease in diameter over time as expected (Figure 1D,E) due to disassembly into their smaller linear fragments, however there was no significant change in the diameter of the core-crosslinked micelles during the experiment. As the micelles were core-crosslinked in situ during the polymerization process, it is likely that the disulfides are embedded deep within the hydrophobic core and thus are not very accessible. GSH is a hydrophilic molecule (log P −6.4), and as such may be unable to penetrate into the hydrophobic inner regions of the micelle to induce complete disassembly of the structure. These observed results may also reflect the high stability and low CAC of the block copolymer assembly.

Finally, in order to investigate the stability of the pHPMAs against protein corona binding, and thus induced aggregation in a protein-rich environment such as within the bloodstream, a DLS study was performed using bovine serum albumin (BSA) as the model protein.[75] Two concentrations of BSA in solution were assayed; 0.2 wt%, which is representative of the protein concentration within DMEM culture media with 10% fetal bovine serum (FBS),[76,77] and 1 wt% to mimic the protein concentration in animal models.[78] It could be seen at the 0.2 wt% BSA concentration that all nanoparticles were stable to aggregation after 24 h incubation at 37 °C, with minimal observable changes in the DLS trace by volume over the course of the experiment (**Figure 2**C; Figure S5, Supporting Information). At the higher concentration of 1 wt%, a similar stability was confirmed for all architectures, with the exception of the Linear-SS. In this case, after incubation with the BSA, the nanoparticle peak was no longer detected by DLS, with only peaks due to the BSA observed. As no large-sized peaks were detected by intensity or volume measurements, this was hypothesized not to be the result of an induced aggregation process, but rather was attributed to interactions between the BSA and the linear polymer obstructing the self-assembly process, resulting in the polymer being present in solution as single chains. Overall, resistance to protein corona binding was observed during the in vitro assays, suggesting the nanoparticles would not be prone to aggregation within biological environments for subsequent assays.

2.4. In Vitro Analysis of Toxicity and Macrophage Uptake

The materials in this work were screened for cytotoxicity in two TNBC cell lines, MDA-MB-231 and MDA-MB-468. In addition, the effects of the polymers on RAW264.7 macrophage cells were also evaluated to further characterize cytotoxicity and gain an insight into immune cell evasion and thus the stealth behavior of the material. For the biological assays, all polymers were labelled with a cyanine5 fluorescent dye through amide coupling with the RAFT terminal carboxylic acid groups. A low incorporation of dye was targeted (≈0.5 per polymer) to reduce any structural impact of the dye molecules on the nanoparticles.[79] Metabolic and lactate dehydrogenase (LDH) release assays in the three cell lines confirmed that no significant toxicity or membrane damage could be observed over all concentrations tested, with cell viabilities remaining close to 100% after 48 h of incubation at concentrations reaching 1 mg mL^{-1} (Figures S6 and S7, Supporting Information).

The stealth behavior in vivo and evasion of uptake by macrophages of the pHPMA materials was initially investigated in an in vitro macrophage model using RAW264.7 cells,[76,80] in order to quantify internalization of the nanoparticles over time, as well as assess any effects of polymer architecture on this behavior. As the pHPMAs were of a range of physical architectures and surface zeta potentials, it was expected that the materials would show a different profile of both time-dependent and concentration-dependent uptake. Indeed, the two smallest polymers, the HB-HPMA-S and HB-SS-HH, demonstrated the most "stealth" behavior, with a very low amount of nanoparticle internalization by macrophages over 4 h (<5 pg per cell). The HB-HPMA-L and Star-SS-L also demonstrated low levels of internalization, with less than 10 pg per cell. In comparison, the larger sized linear and micellar pHPMAs showed a significantly higher macrophage uptake over this time period (≈20 pg per cell), further suggesting a size dependence for this process. Particularly, it can be seen that there is a difference in the initial rate of uptake over the first 60 min (Figure 2B) for the different polymers, with the Linear-SS and Micelle-SS showing the greatest increase, or rate of uptake, during this period. The observed size dependency of cellular uptake could be attributed to several phenomena; firstly the small nanoparticles evading recognition by surface receptors on the macrophages, and in turn decreased susceptibility to phagocytosis.[81] Second, the smaller sized particles (≤15 nm) may be internalized into macrophages via fewer pathways than the larger particles. For example, clathrin- and caveolin-mediated endocytosis have been

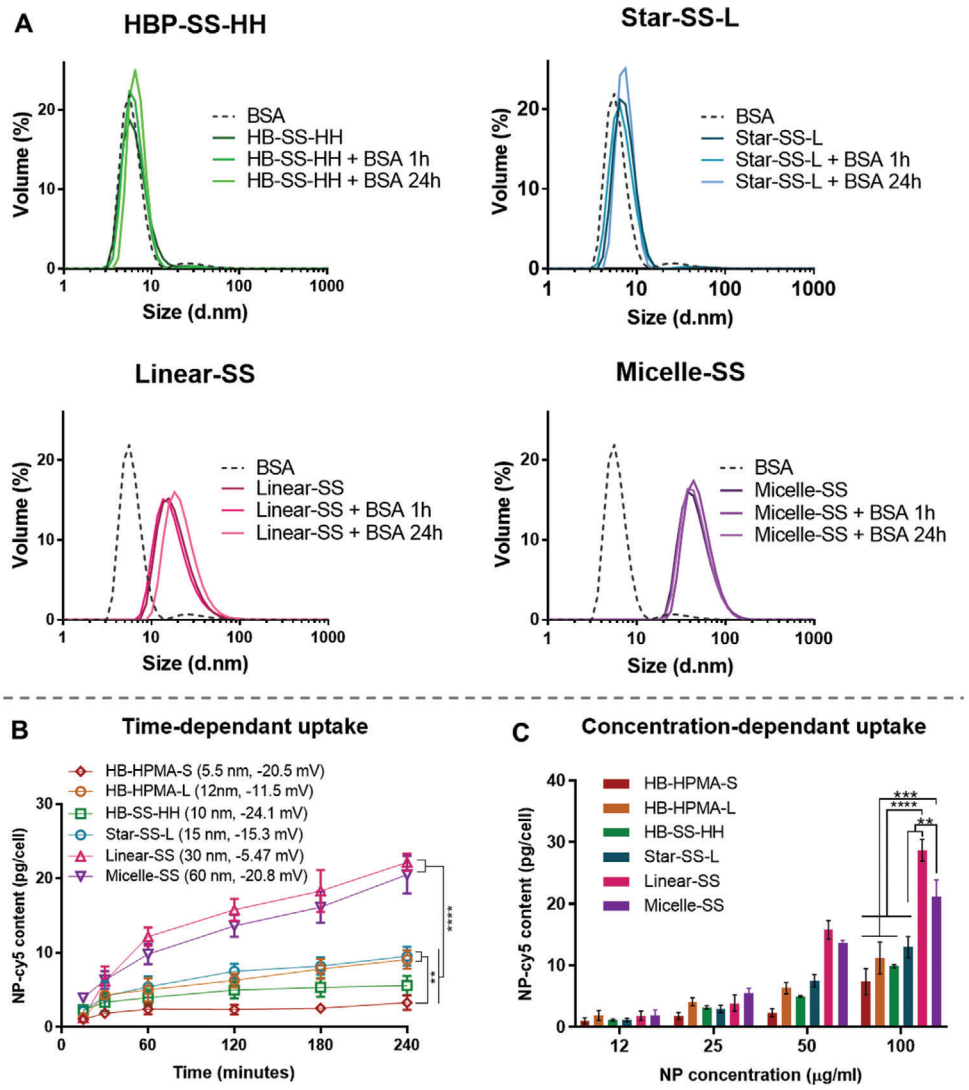

Figure 2. Protein corona binding studies of pHPMAs with A) representative DLS traces of the redox-responsive polymer architectures after incubation in 0.2 wt% of BSA, confirming stability to aggregation in these conditions. In vitro data depicting B) time-dependent uptake of degradable pHPMAs into RAW264.7 macrophages at a concentration of 50 μg mL^{-1} and C, and B) concentration-dependent uptake of degradable pHPMAs after 2 h incubation.

reported to be restricted with small nanoparticles (<50 nm),[82] and this is believed to be a result of insufficient thermodynamic driving force for membrane wrapping.[83–85] To obtain increased driving force to exploit these endocytotic routes, such as that demonstrated by the larger nanoparticles, the smaller nanoparticles must cluster or aggregate,[82] however stability studies in cell culture conditions (Figure 2) indicate pHPMA materials are unlikely to do so.

It is interesting to note that the highest uptake in both time and concentration-dependence was not observed for the largest nanoparticles (micelle), but for the linear architecture, reflecting the results of the BSA assay (Figure 2). Despite having a smaller size of 30 nm, the zeta potential is −5.47 mV in comparison to the −20.8 mV for the 60 nm micelle, and thus indicates, in agreement with previous literature, that there is an influence of both particle size and surface charge in reducing macrophage association, and so a balance between the two factors must be achieved for stealth behavior (Figure S8, Supporting Information).[86] Fluorescence microscopy images of the macrophages confirmed that the observed uptake was intracellular rather than membrane association (Figure S9, Supporting Information).

2.5. In Vivo Analysis of Organ Distribution

In vivo biodistribution studies were performed in healthy female nude mice to characterize the effects of size and shape on organ accumulation, particularly focusing on organ distribution within clearance pathways such as the liver and kidneys. After intravenous administration of each material, mice were imaged in vivo at 1, 4, and 24 h postinjection, and at each time point, two mice in each group were culled and their organs were imaged ex vivo. Representative in vivo images at 4 h postinjection are depicted in **Figure 3**A, where it can be seen for the two

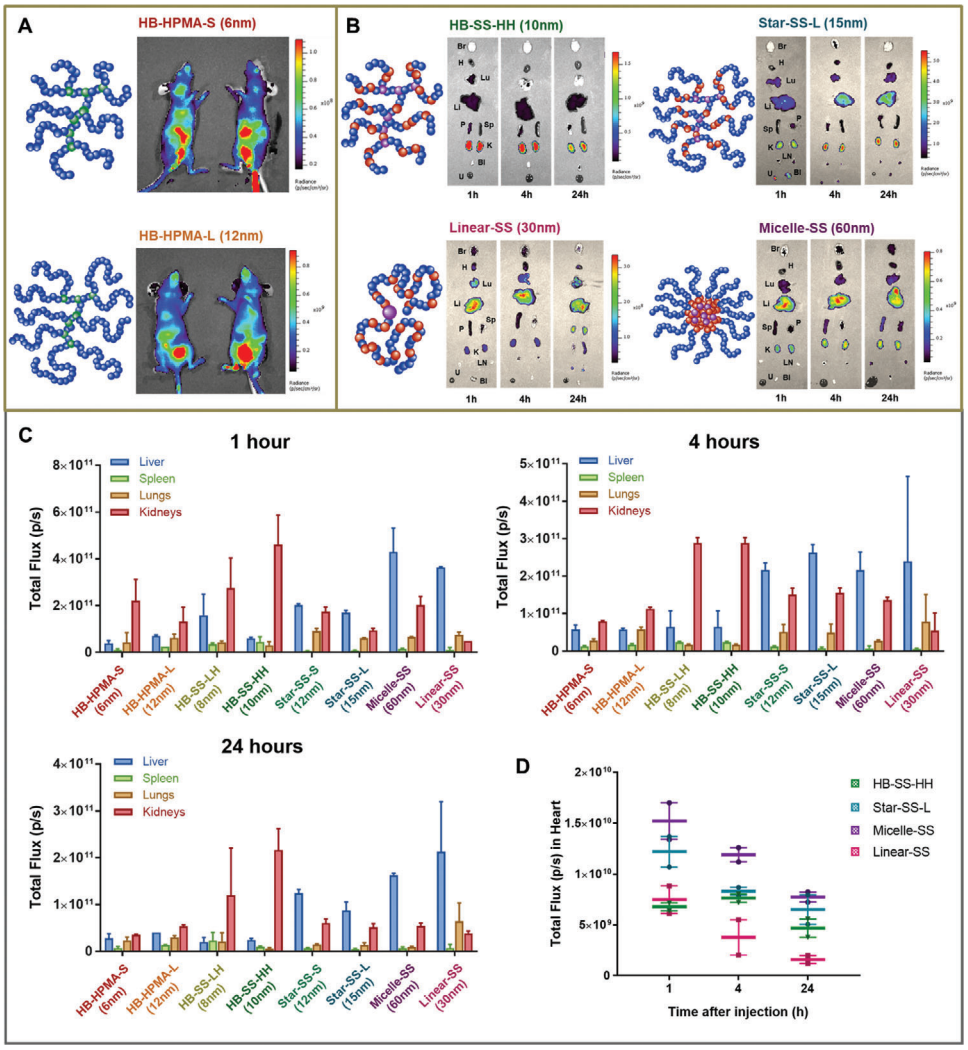

Figure 3. A) Representative in vivo images at 4 h postinjection for the nondegradable hyperbranched polymers. B) Representative ex vivo images of redox-responsive pHPMA materials at 1, 4, and 24 h postinjection (Br: brain; H: heart; Lu: lungs; Li: liver; P: pancreas; Sp: spleen; K: kidneys; U: urine; Bl: blood). C) Quantitation of the ex vivo organ data to allow comparison between different architectures, highlighting the fluorescence signal in organs important for nanoparticle clearance from the bloodstream ($n = 2 \pm$ SD) over time. D) Quantitation of the fluorescence signal in the heart at all times, indicative of circulating nanoparticles ($n = 2 \pm$ SD).

nondegradable control polymers, HB-HPMA-S and HB-HPMA-L, that at this time point there is evidence of clearance of the polymeric materials through the renal system, characterized by fluorescent signal within the kidneys and bladder of the mice.

Due to tissue penetration limits of in vivo fluorescence imaging, which limits detailed observation of organ fluorescence in vivo,[87] the ex vivo images at each time point were also analyzed. Representative ex vivo images of the redox-responsive polymer architectures are shown in Figure 3B.

There were obvious variations in the distribution of fluorescence signal throughout the different organs after administration of the polymers, dependent on the architecture, physical size and surface charge of the materials. The linear polymers, which were of the highest molecular weight (≈250 kDa) showed high accumulation of signal in the liver, with the least observed fluorescence in the kidneys of all the polymers. As the Linear-SS polymer contained only a single disulfide breaking point, the smallest possible polymer fragment was likely to be ≈125 kDa in size, and previous literature has shown that linear polymers with molecular weights over 50 kDa show reduced renal filtration and enhanced liver uptake.[88] In contrast, for the hyperbranched polymers, which had the lowest molecular weight and physical size, the intensity of fluorescent signal was greatest in the kidney and with low liver fluorescence. For the star and micelle materials, the signal in the liver was increased over that of the hyperbranched polymers; however, kidney fluorescence was also observed for both architectures. To probe further the distribution of the pHPMA materials through the various organs, regions of interest (ROI) were drawn around the ex vivo images for semiquantitation. It is important to note that fluorescence imaging in tissues is only semiquantitative, and therefore fluorescence signal was expressed as total flux (the radiance (photons/sec) in each pixel integrated over the ROI area) in order to improve the interpretation of the results. As the organs of most interest were those

involved in clearance of nanoparticles from the bloodstream, the data for kidneys, liver, spleen, and lungs are presented at each time point (Figure 3C).

The ROI analysis was able to confirm the qualitative observations from the ex vivo images, depicting clear changes in organ distribution across the different pHPMA materials. For the smallest nondegradable HB-HPMA-S, polymer accumulation was observed to be mostly confined within the kidneys, with some evidence of accumulation in the liver as well. This suggests that the materials were being primarily cleared through the renal system, which was as expected for small and flexible nanomaterials.[71,89] For the larger HB-HPMA-L, this effect was slightly delayed, likely due to the physical size of 12 nm moving the materials further beyond the theoretical renal clearance threshold of ≈6 nm.[90] For the degradable HBs, it can be seen that all mononuclear phagocytic system (MPS) organs showed a low amount of fluorescence, with the majority of the fluorescence found in the kidneys throughout the course of the experiment. The two redox-responsive hyperbranched polymers, HB-SS-LH ($D_H \approx 8$ nm) and an HB-SS-HH ($D_H \approx 10$ nm), were comparable in size to the nondegradable HB-HPMA-S ($D_H \approx 6$ nm) and HB-HPMA-L ($D_H \approx 12$ nm); however, they demonstrated reduced MPS organ accumulation and increased renal filtration in comparison. This may have been due to fragmentation of the degradable polymers by reducing species in the body and subsequent renal clearance, or by avoidance of micropinocytosis by MPS-resident macrophages. The latter hypothesis is in accordance with the in vitro macrophage uptake, where the HB-SS-HH materials showed the least uptake in experiments in which both time-dependent and concentration-dependent internalization were evaluated.

For the larger pHPMAs, which contained fewer disulfide links as well as larger fragments following disassembly as seen by DLS, the ratio of MPS to renal accumulation increased. The highest liver uptake was seen for the self-assembled nanoparticles of the Linear-SS polymer, which was again in accord with the in vitro assays of high macrophage internalization, despite the initial particle size falling within the middle of the size range in this study (30 nm).[91] For this polymer, a high proportion (≈50–70% of the fluorescence signal) appeared in the liver as well as the lungs at all time points, with only minimal signal coming from the kidneys (less than 20% of the signal relative to the other organs) These data may be suggestive of interactions with serum proteins (as observed in the in vitro assays with BSA at high protein concentrations; Figure S5, Supporting Information), which is known to result in recognition by macrophages of the MPS, and thus this polymer was more likely to have increased liver uptake in vivo.[92] The Star-SS-S ($D_H \approx 12$ nm) and Star-SS-L ($D_H \approx 15$ nm) both showed increased accumulation in the liver rather than the kidneys, despite being synthesized from the 8 nm HB-SS-HH core. This suggests that the covalent attachment of a larger pHPMA corona reduced the ability of the materials to filter through the renal system, even after cleavage of the disulfide crosslinks. For the largest particles, the Micelle-SS ($D_H \approx 60$ nm), the highest uptake was in the liver but there was observable signal in the kidneys at all time points, and an overall behavior ratio comparable to the Star-SS materials. This is indicative of disassembly in vivo into single polymer chains and subsequent renal clearance, even though the prior in vitro experiments with glutathione did not result in micellar breakdown over the same time period. It is likely therefore that the kidney accumulation can be attributed to dilution of the micelles below the CMC in vivo during circulation, despite the covalent crosslinking, resulting in an equilibrium shift toward single polymer chains which were then cleared through the renal system.[93]

It has been reported that the lungs, liver and spleen are the important sites for nanoparticle clearance by phagocytosis from the bloodstream, and it can be seen from the ex vivo data that the spleen signal for all materials was extremely low across all time points, even for materials that were retained in the liver.[81,94,95] Furthermore, nanoparticle aggregation or agglomeration in vivo typically results in significant amounts of accumulation within the lungs, however it can be seen that lung signal was also low (and less than 20% of the fluorescence as estimated from the optical imaging) for all materials. These data together imply that all the pHPMAs investigated were not prone to immune-mediated uptake and protein-induced aggregation within the bloodstream, and thus could be considered as candidate stealth nanoparticle drug carriers for drug delivery.

Finally, the fluorescence signal within the heart was evaluated as a proxy for detecting circulation of nanoparticles within the body.[96] Figure 3D and Figure S10 (Supporting Information) show representative signal over time for the pHPMAs, and we were particularly interested in HB-SS-HH, Star-SS-L, Micelle-SS, and Linear-SS. Clear differences in circulation lifetimes were observed across these samples. The smallest HB-SS-HH showed the most rapid clearance from the heart, in line with the high kidney signal also observed. Unsurprisingly the larger Micelle-SS showed more prolonged retention in the circulation, while the Linear-SS showed clearance likely due to opsonization as already discussed. It was also of note that the Star-SS-L polymer showed good circulation lifetime despite its small physical size, whereby minimal organ accumulation was detected at the first time point indicating it was still in circulation, with significant fluorescence signal still detected within the heart after 24 h.

2.6. Doxorubicin Conjugation to Candidate pHPMAs

Based on the biodistribution data, two candidate pHPMA architectures were selected for investigation as drug delivery carriers: HB-SS-HH ($D_H \approx 10$ nm) and Star-SS-L ($D_H \approx 15$ nm), as these two materials were of essentially the same chemical composition and similar size, but exhibited very different organ accumulation and circulation lifetime behavior. We were particularly interested if these features might allow us to factor out particle size and chemistry in terms of tissue penetration, and focus on how biodistribution might then alter ultimate therapeutic effect. In this way, the selection of the two nanoparticles of similar size but very different in vivo behaviors had potential to give intriguing insights given that only one variable was being significantly modified (polymer architecture). The Boc-protecting groups on the *t*BHM units within each polymer structure were removed through trifluoroacetic acid (TFA) deprotection, and then DOX was attached through the formation of an acid-labile hydrazone bond to yield the polymer prodrugs (**Figure 4**A; Figure S11, Supporting Information). Following purification, quantification of DOX conjugation was calculated using NMR

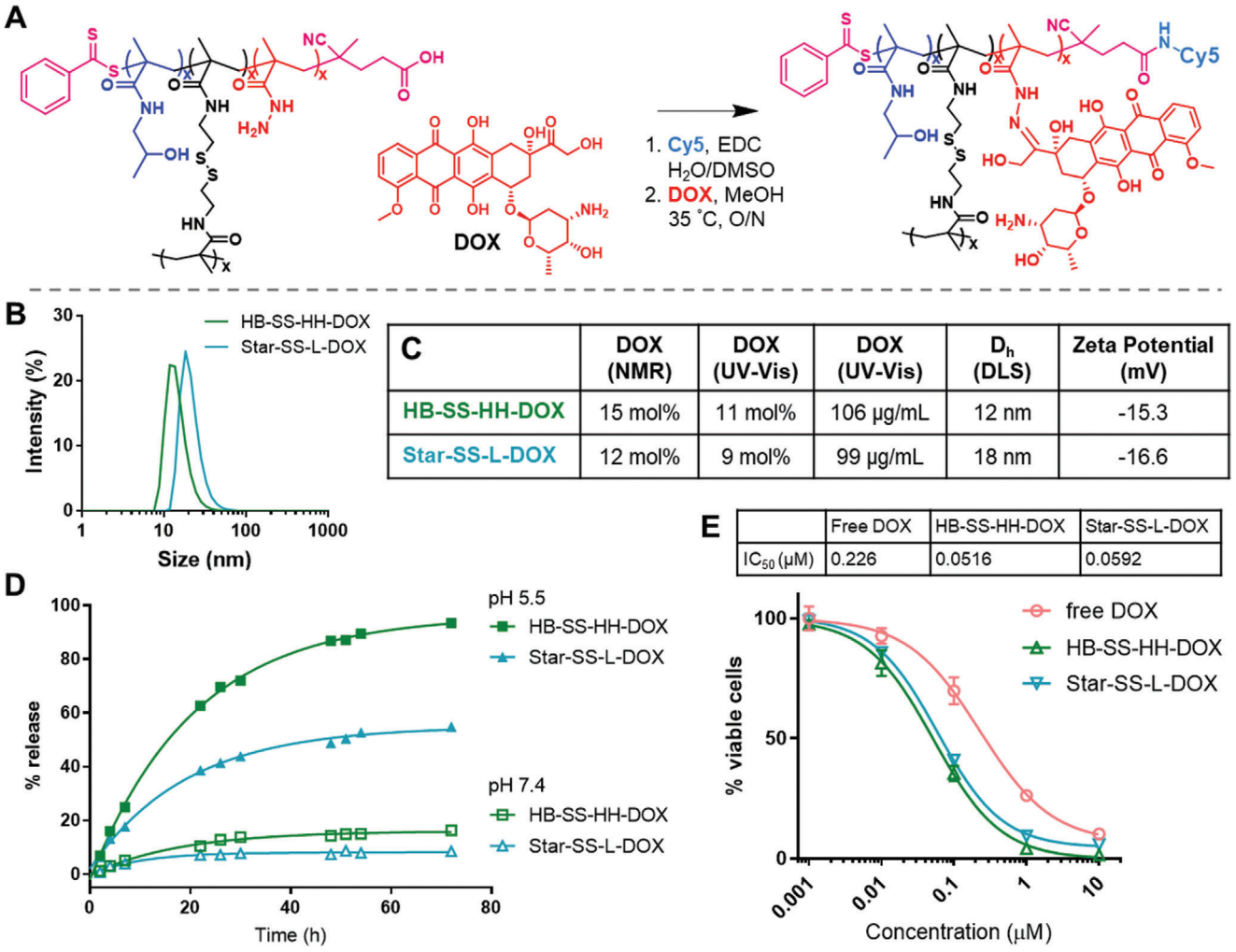

Figure 4. A) Synthetic scheme for the boc-deprotection and DOX attachment to a representative pHPMA, B) DLS traces of the polymer prodrugs, C) quantification of DOX attachment by NMR and UV–vis (488 nm) and characterization by DLS, D) stability and release of DOX from the polymer prodrugs at pH 5.5 and 7.4 conditions, and E) growth inhibition curves of free DOX and the polymer prodrugs against MDA-MB-231 cells after 48 h incubation.

spectroscopy to integrate the signals from the drug compared with the polymer backbone (Figure S12, Supporting Information) and UV–vis analysis using a standard curve of DOX·HCl (Figure S13, Supporting Information), which revealed functionalization in the range of 9–12 mol% (Figure 4C). The polymer prodrugs were sized by DLS, giving size values of approximately D_H = 12 nm for HB-SS-HH-DOX and D_H = 18 nm for Star-SS-L-DOX, indicating a slight increase in the hydrodynamic volume as a result of the drug attachment (Figure 4B). The stabilities of the polymer prodrugs were assessed through the DMEM and BSA assays described above, which confirmed that the presence of the DOX within the nanoparticle structure did not have any impact on the stability, with both particles remaining as discrete populations in both conditions over 48 h (Figure S14, Supporting Information). Finally, an in vitro buffer release experiment was conducted to determine the stability of the drug conjugation, as well as their DOX release kinetics under physiologically relevant conditions of pH. Each nanoparticle was dialyzed in either pH 5.5 (endosome conditions) or 7.4 (serum conditions) phosphate buffer at 37 °C for 72 h, and the buffer measured at periodic intervals for DOX concentration. Quantification of DOX release showed that at pH 7.4 the prodrugs released up to 10% over the time frame of the experiment, however this value increased to 55% for the Star-SS-L-DOX and up to 95% for the HB-SS-HH-DOX, with no burst release and calculated half-lives of ≈14 h (Figure 4D).

2.7. In Vitro Analysis of Drug Delivery Efficacy in 2D and 3D Models

The ability for the polymer prodrugs to successfully deliver DOX into cells, and any variations that resulted from different architectures, was evaluated in the MDA-MB-231 TNBC cell line. Dose-response curves of DOX toxicity were produced over 48 h incubation at varying concentrations of free drug and both drug-loaded nanoparticles. It can be seen in Figure 4E that the attachment of DOX to the nanoparticles resulted in a significantly

improved therapeutic effect, with a decrease in the half maximal inhibitory concentration (IC_{50}) values from 0.23×10^{-6} M for free DOX to 0.059×10^{-6} and 0.051×10^{-6} M for the HB-SS-HH-DOX and Star-SS-L-DOX respectively. MDA-MB-231 cells have been demonstrated to exhibit resistance to doxorubicin, this improvement in efficacy was hypothesized to be the result of more specific trafficking of the drug into the cells and thus an increased DOX intracellular concentration.[97–99] Cellular uptake studies evaluating polymer internalization via fluorescence microscopy suggested that DOX trafficked to intracellular compartments when attached to polymers in a manner different to those of the free drug (Figure S15, Supporting Information). After 1 h incubation of HB-SS-HH-DOX in MDA-MB-231 cells, colocalization of the cyanine5 (Cy5) and DOX signals was observed, with observed punctate staining indicative of active internalization pathways and discrete intracellular locations, confirming that the nanoparticles were able to deliver the doxorubicin to vesicular compartments within the cells. Images at 2 and 4 h of uptake suggested delivery of doxorubicin into the nucleus through cleavage of the hydrazone bond; at 2 h some doxorubicin signal was observed in the nucleus and by 4 h the doxorubicin was almost entirely in the nucleus. Further magnification at 2 h of uptake confirmed these observations, with clear endosomal staining of both Cy5 and DOX and also signals of doxorubicin within the nucleus colocalizing with the 4′,6-diamidino-2-phenylindole (DAPI) stain (Figure S16, Supporting Information).

In order to investigate the ability of the polymer prodrugs to improve delivery of DOX within more tissue-like environments, a 3D spheroid culture model was used. 3D spheroid models are more representative of the tumor environment in vivo, and allow the effects of cell–cell interactions and the dense extracellular matrix (ECM) network typically observed in solid tumors to be evaluated for their impact on nanoparticle delivery. Accordingly, 3D spheroids of MDA-MB-231 were cultured for 4 days and confirmed by optical imaging (**Figure 5**A). The spheroids were dosed with blank NPs, free DOX or the polymer prodrugs and images of the spheroids were taken daily for quantification of growth or growth inhibition through volume analysis, and after 72 h overall cytotoxicity was evaluated (Figure S18, Supporting Information).

It can be seen in Figure 5A that for the control spheroids, which received no treatment, the 3D mass continued to grow over the course of the experiment reaching over 100% volume increase. Nondrug loaded nanoparticles, as expected, showed no toxicity and no inhibition of spheroid growth (Figure S17, Supporting Information). Free DOX was able to inhibit the growth of the spheroids at a concentration of 1×10^{-6} M after 72 h, and from the optical images it was observed that this reduction in volume was due to cell death on the periphery of the spheroids. Importantly, both HB-SS-HH-DOX and Star-SS-L-DOX were observed to inhibit spheroid growth at a lower concentration than the free drug, at 0.01×10^{-6} and 0.1×10^{-6} M in DOX, respectively. Of particular significance, at the highest concentration tested (10×10^{-6} M), the polymer prodrugs were able to induce complete destruction of the spheroid structure, a phenomenon not observed for the free drug. This gave further confirmation of the ability not only for the nanoparticles to deliver doxorubicin into the cells, but also to penetrate deep within a tumor-like solid mass to ensure cell kill beyond the surface layers and subsequent loss of spheroid structure. Interestingly, the two polymer prodrugs showed comparable behavior, with IC_{50} values in the 3D model of 0.36×10^{-6} M for the HB-SS-HH-DOX and 0.52×10^{-6} M for the Star-SS-L-DOX (Figure 5C). These results suggested that despite the slower drug release profile of the Star-SS-L-DOX in buffer conditions and the reduced IC_{50} value in the 2D monolayer model, this nanoparticle was still efficacious in a 3D model.

2.8. Assessment of Drug Delivery Efficacy in a Murine Orthotopic Model of Triple Negative Breast Cancer

Based on these promising results, in vivo therapeutic efficacy studies were performed. An orthotopic model of TNBC was established in female nude mice using MDA-MB-231 cells transfected with luciferin, to provide bioluminescence imaging as well as physical measurements of tumor growth over time. Once palpable tumors were confirmed, mice were dosed according to two regimes. In the first schedule, the mice were dosed 3× a week for 2 weeks at a value of DOX (as free drug or as dosed equivalent) of 4 mg kg^{-1} (Figure 5D). In the second schedule, the mice were dosed three times in the first week, and then 1× per week for the next 2 weeks, at a value of DOX (as free drug or as dosed equivalent) of 2 mg kg^{-1} (Figure 5E,G). For both experiments, mice were observed daily for adverse effects, body mass and tumor volumes, continuing for a further 2 weeks following the treatment period. At 28 days after the initial dosing, all mice were culled and the final tumors analyzed, as well as the hearts and spleens as indicators of systemic DOX toxicity. As apparent from Figure 5D, in the first schedule all treatment regimens reduced tumor growth relative to vehicle control, but the Star-SS-L-DOX was less effective than HB-SS-HH-DOX and free DOX alone.

It can be seen from Figure 5E that for the second schedule, again all treatment regimens reduced tumor growth relative to vehicle control, however in this case both nanoparticle treatment groups were able to improve on the therapeutic effect of the free drug, reducing tumor growth to 138% for the HB-SS-HH-DOX ($p^* < 0.05$ vs free DOX) and 127% for the Star-SS-L-DOX ($p^{**} < 0.01$ vs free DOX). We attribute the difference in relative efficacies of the polymers in the two studies to the different time periods in between dosing, and their likely distributions throughout the body in comparison with the free doxorubicin. It is known that in humans doxorubicin has a triphasic distribution profile owing to plasma protein binding, but studies have reported that more than 90% of the injected dose is eliminated within a day.[100] For mice, a similar percentage of free doxorubicin is lost within 12 h, thus a more frequent 48 h dosing schedule, as that shown in Figure 5D, was likely to result in greater drug concentrations in the tumors compared to the 3–4 day dosing interval study, as shown in Figure 5E. In addition, as the dose of doxorubicin was lowered to 2 mg kg^{-1} in the experiments reported in Figure 5E, the tumors likely received a much lower dose, resulting in limited ability to reduce the tumor volume. By contrast, the longer circulating polymer pro-drugs were relatively more effective at preventing tumor growth than free doxorubicin in the longer-interval dosing study, which is consistent with previous literature on pHPMA–DOX conjugates.[41,101–103]

We considered it likely that the nanoparticle dosed groups could achieve a longer residence time within the tumor mass than the free drug; indeed, after the dosing period the tumors

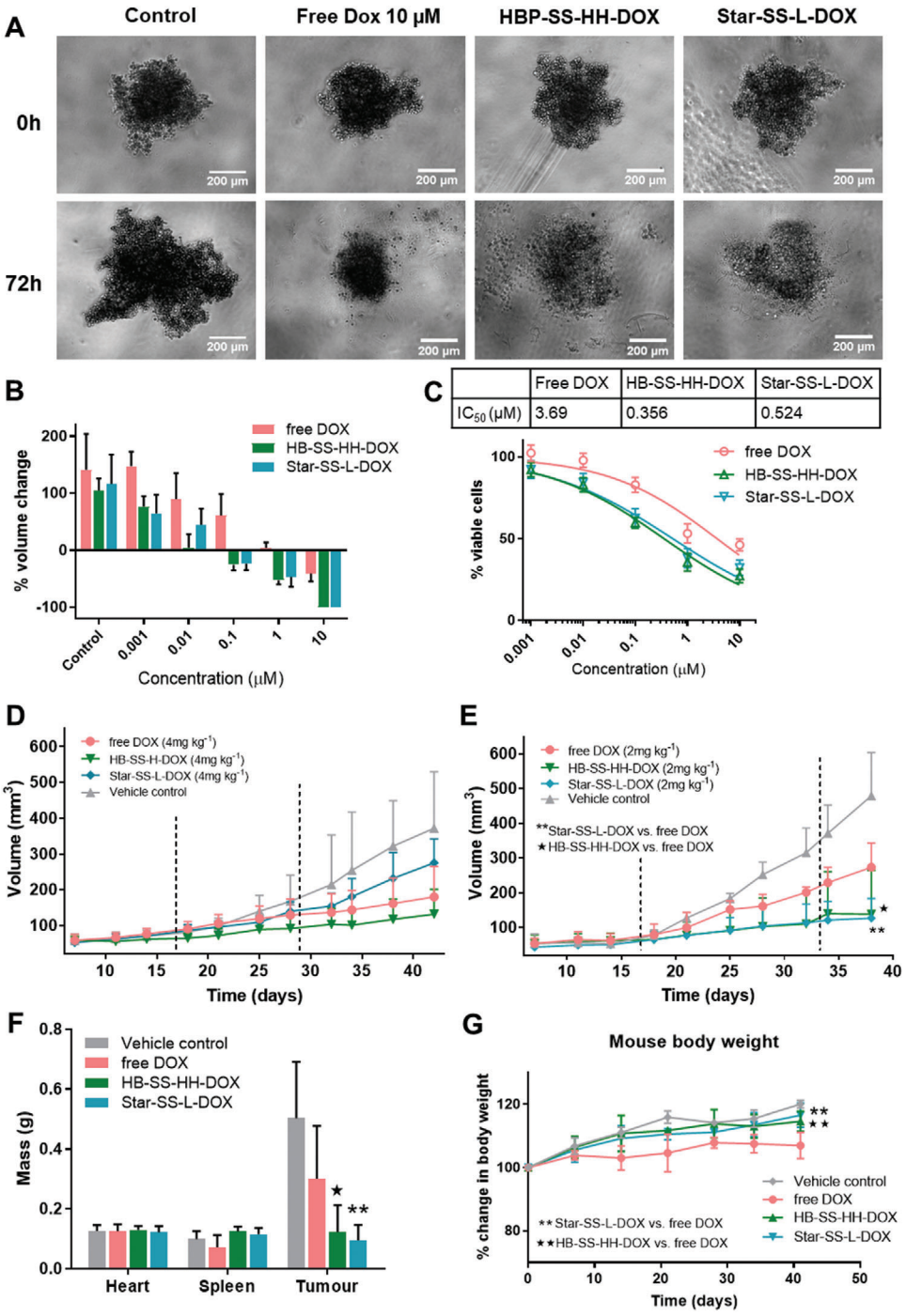

Figure 5. A) Optical microscopy images of MDA-MB-231 spheroids at 4 and 7 day incubation after control (no treatment), free DOX and polymer prodrug treatments, B) %volume change of spheroids between 0 and 72 h incubation based on volume analysis, and C) spheroid growth inhibition curves of free DOX and the polymer prodrugs after 72 h incubation. Orthotopic model of TNBC was established in female nude mice using MDA-MB-231 cells transfected with luciferin D) 4 mg kg^{-1} dosing: in vivo tumor volumes as measured by calipers after frequent dosing (every 2 days for 2 weeks) and E) 2 mg kg^{-1} dosing: tumor volumes as measured by calipers for the wider dosing interval study (5 doses over 3 weeks). The dotted lines indicate the dosing period. F) masses of key organs relative to tumor are given for the wider dosing interval study and G) mouse body weights throughout the wider interval dosing study.

in the DOX group continued to grow, however both the HB-SS-HH-DOX and Star-SS-L-DOX groups showed a far slower rate of regrowth in this recovery period. The ex vivo analyses of tumor mass and volume showed that the tumors from both nanoparticle treatment groups were significantly smaller than those treated with free DOX (Figure 5F). To provide further insights, a 24 h biodistribution study of both nanoparticle groups confirmed fluorescent signal, and thus localization, within the regions of the tumors after 24 h, providing supporting evidence of the DOX efficacy (Figure S19, Supporting Information).

A key driver in the development of nanomedicines for cancer drug delivery is evaluation of the systemic toxicity as a result of the administered drug. The toxicity can be evaluated via measurements of body mass in experimental animals, and more relevantly to human doxorubicin use by evaluating mass changes in the heart and spleen.[104,105] The data in Figure 5F show that the body mass of the DOX treatment group increased at a slower rate than all other groups, only reaching 106% of their original body mass over the course of 28 days, in comparison to ≈115% for both nanoparticle dosed groups, in agreement with prior literature.[106–109] In addition, there was some evidence of decrease in the average mass of the spleen in the mice of the doxorubicin group, which is another indication of drug toxicity that was not present in any other experimental groups (Figure 5F). These results suggested that the polymer prodrugs did not cause DOX release during circulation to a detrimental extent, and therefore did not impart nonspecific toxicity to the animals.

When the orthotopic model data is considered as a whole, the most intriguing observations were those revealing the difference in efficacy between HB-SS-HH-DOX and Star-SS-L-DOX over the different dosing regimens. While both formulations exhibited very similar potencies in 3D spheroids, in vivo HB-SS-HH-DOX (D_H = 12 nm) had been shown to accumulate more in the kidneys while Star-SS-L-DOX (D_H = 18 nm) was more retained in the liver (Figure 3B,C), and drug release was faster from the HB-SS-HH-DOX than the Star-SS-L-DOX polymers (Figure 4D). It is likely that the better efficacy of HB-SS-HH-DOX in the first dosing regime was due to a higher doxorubicin dose reaching the tumors on account of the longer circulation time compared to the free drug and the faster release from the carrier compared to the Star-SS-L-DOX. In the latter case, it is likely that increasing the dose made no difference to the efficacy as even at the higher amounts administered, the release of DOX was not sufficient to generate the same amount of drug in the tumors as that of HB-SS-HH-DOX. Thus, the change in efficacy of the polymers compared to free drug at higher drug equivalents administered (Figure 5D: 4 mg kg^{-1} compared to 5E: 2 mg kg^{-1}), which at first seems counter-intuitive, can be at least partly explained by the difference in the in vivo residence times of the drugs and carriers, and by the different release rates from the carriers. In turn, the different architectures of the HB-SS-HH-DOX and Star-SS-L-DOX polymers can account for the altered rate of doxorubicin release, as the cleavage of the hydrazone bond required penetration of acidic media into the core of the polymers, and an initial influx of GSH to "open up" the polymer network by cleaving the disulfide links maintaining the chains together.

These data highlight the complexities of responsive polymer structure, conformation, biodistribution and drug release profiles pertaining to anticancer efficacy. They also indicate the important trade-off between nanoparticle size to achieve both prolonged circulation and good penetration into a solid tumor mass, and the effects that changing polymer architectures can have in altering biodistribution and drug release even when the underlying chemistries are almost identical. The extensive data in this study provide key pointers to polymer design such that drug release rates can be "dialled in," dosing schedules can be planned which maximize the therapeutic effects of the formulations while reducing systemic toxicity and as such the ability to program drug release and biodistribution from fine control of polymer architecture is extremely promising for future delivery studies.

3. Conclusions

Here, the effect of size and 3D architecture of identical underlying chemistries pHPMA materials on in vitro transport and in vivo organ accumulation was investigated. Through aqueous RAFT polymerization, we successfully produced a small set of polymer materials spanning a size range from 5 to 60 nm, with linear, hyperbranched, star, and self-assembling micellar architectures, allowing for investigation of the contribution of architecture, size and degradability on in vivo particle distribution by maintaining the same materials chemistry throughout. The resulting materials showed promising behavior as stealth carriers both in vitro and in vivo. In vitro macrophage uptake studies demonstrated significantly different behaviors governed by surface zeta potential and physical size. The smaller hyperbranched structures were taken up by macrophages to a significantly lower degree than the larger hyperbranched and star particles, in agreement with reduced MPS uptake and increased renal clearance in vivo. Conversely, the larger self-assembled micelles and linear polymers were more recognized by macrophages in vitro and showed higher MPS/renal clearance ratios in vivo. Functionalization of two lead nanoparticles, HB and Star, with a model anticancer drug doxorubicin validated the promise of the nanoparticles in this work for drug delivery applications. Both polymer prodrugs had improved efficacy over free drug in 2D and 3D cell culture models and, when dosed at appropriate schedules, in an orthotopic model of human TNBC in mice. These are promising results for the polymer-drug conjugates in this work in terms of preclinical efficacy in an aggressive cancer model, justifying future investigations in comparison with current clinical standards of care formulations such as Doxil, to better inform design of the investigated carriers to aid practical application and potential translation. By tuning polymer structures to assemble into different conformations and then disassemble into specific size ranges, we have shown it is possible to direct materials of essentially the same chemistries into different cellular and physiological regions, and thus open new routes to targeted nanomaterial diagnostics and/or therapeutics.

Supporting Information

Supporting Information is available from the Wiley Online Library or from the author.

Acknowledgements

The animal experiments were approved by the UK Home Office under the Licence number PPL P435A9CF8. This work was supported by

the Engineering and Physical Sciences Research Council (Grant Nos. EP/N006615/1, EP/N03371X/1, EP/H005625/1, and EP/L013835/1). This work was also funded by the Royal Society (Wolfson Research Merit Award WM150086) to C.A. The authors thank the Nanoscale and Microscale Research Centre (nmRC) for providing access to instrumentation.

Data Access Statement

All relevant data are available from the University of Nottingham's Research Data Management Repository or on request via cameron.alexander@nottingham.ac.uk'

Conflict of Interest

The authors declare no conflict of interest.

Keywords

biomedical applications, bionanotechnology, drug delivery, polymeric materials, stimuli-responsive materials

Received: May 27, 2020
Revised: September 16, 2020
Published online:

[1] R. Duncan, M. J. Vicent, *Adv. Drug Delivery Rev.* **2010**, *62*, 272.
[2] L. Zhang, F. X. Gu, J. M. Chan, A. Z. Wang, R. S. Langer, O. C. Farokhzad, *Clin. Pharmacol. Ther.* **2008**, *83*, 761.
[3] O. C. Farokhzad, R. Langer, *ACS Nano* **2009**, *3*, 16.
[4] A. A. Manzoor, L. H. Lindner, C. D. Landon, J.-Y. Park, A. J. Simnick, M. R. Dreher, S. Das, G. Hanna, W. Park, A. Chilkoti, G. A. Koning, T. L. M. ten Hagen, D. Needham, M. W. Dewhirst, *Cancer Res.* **2012**, *72*, 5566.
[5] D. Liu, C. R. Bernuz, J. Fan, W. Li, A. Correia, J. Hirvonen, H. A. Santos, *Adv. Funct. Mater.* **2017**, *27*, 1604508.
[6] J. Wan, Y. Qiao, X. Chen, J. Wu, L. Zhou, J. Zhang, S. Fang, H. Wang, *Adv. Funct. Mater.* **2018**, *28*, 1804229.
[7] H. Huang, J. F. Lovell, *Adv. Funct. Mater.* **2017**, *27*, 1603524.
[8] O. M. Koo, I. Rubinstein, H. Onyuksel, *Nanomedicine* **2005**, *1*, 193.
[9] M. Wang, M. Thanou, *Pharmacol. Res.* **2010**, *62*, 90.
[10] L. Tang, X. Yang, Q. Yin, K. Cai, H. Wang, I. Chaudhury, C. Yao, Q. Zhou, M. Kwon, J. A. Hartman, I. T. Dobrucki, L. W. Dobrucki, L. B. Borst, S. Lezmi, W. G. Helferich, A. L. Ferguson, T. M. Fan, J. Cheng, *Proc. Natl. Acad. Sci. USA* **2014**, *111*, 15344.
[11] J. Wang, W. Mao, L. L. Lock, J. Tang, M. Sui, W. Sun, H. Cui, D. Xu, Y. Shen, *ACS Nano* **2015**, *9*, 7195.
[12] A. Reisch, D. Heimburger, P. Ernst, A. Runser, P. Didier, D. Dujardin, A. S. Klymchenko, *Adv. Funct. Mater.* **2018**, *28*, 1805157.
[13] J. Shi, P. W. Kantoff, R. Wooster, O. C. Farokhzad, *Nat. Rev. Cancer* **2017**, *17*, 20.
[14] A. Albanese, P. S. Tang, W. C. W. Chan, *Annu. Rev. Biomed. Eng.* **2012**, *14*, 1.
[15] J. Cui, R. De Rose, K. Alt, S. Alcantara, B. M. Paterson, K. Liang, M. Hu, J. J. Richardson, Y. Yan, C. M. Jeffery, R. I. Price, K. Peter, C. E. Hagemeyer, P. S. Donnelly, S. J. Kent, F. Caruso, *ACS Nano* **2015**, *9*, 1571.
[16] J. Ji, F. Ma, H. Zhang, F. Liu, J. He, W. Li, T. Xie, D. Zhong, T. Zhang, M. Tian, H. Zhang, H. A. Santos, M. Zhou, *Adv. Funct. Mater.* **2018**, *28*, 1801738.
[17] J. J. Arroyo-Crespo, C. Deladriere, V. J. Nebot, D. Charbonnier, E. Masiá, A. Paul, C. James, A. Armiñán, M. J. Vicent, *Adv. Funct. Mater.* **2018**, *28*, 1800931.
[18] E. Blanco, H. Shen, M. Ferrari, *Nat. Biotechnol.* **2015**, *33*, 941.
[19] D. L. Jasinski, H. Li, P. Guo, *Mol. Ther.* **2018**, *26*, 784.
[20] Y. Wei, L. Quan, C. Zhou, Q. Zhan, *Nanomedicine* **2018**, *13*, 1495.
[21] P. C. Ke, S. Lin, W. J. Parak, T. P. Davis, F. Caruso, *ACS Nano* **2017**, *11*, 11773.
[22] M. J. Roberts, M. D. Bentley, J. M. Harris, *Adv. Drug Delivery Rev.* **2012**, *64*, 116.
[23] R. B. Greenwald, Y. H. Choe, J. McGuire, C. D. Conover, *Adv. Drug Delivery Rev.* **2003**, *55*, 217.
[24] P. Zhang, F. Sun, S. Liu, S. Jiang, *J. Controlled Release* **2016**, *244*, 184.
[25] C. Li, S. Wallace, *Adv. Drug Delivery Rev.* **2008**, *60*, 886.
[26] B. Romberg, J. M. Metselaar, L. Baranyi, C. J. Snel, R. Bünger, W. E. Hennink, J. Szebeni, G. Storm, *Int. J. Pharm.* **2007**, *331*, 186.
[27] N. Adams, U. S. Schubert, *Adv. Drug Delivery Rev.* **2007**, *59*, 1504.
[28] C.-H. C.-H. Wang, C.-H. C.-H. Wang, G.-H. Hsiue, *J. Controlled Release* **2005**, *108*, 140.
[29] K. Maruyama, S. Okuizumi, O. Ishida, H. Yamauchi, H. Kikuchi, M. Iwatsuru, *Int. J. Pharm.* **1994**, *111*, 103.
[30] C. Siegers, M. Biesalski, R. Haag, *Chem. – Eur. J.* **2004**, *10*, 2831.
[31] L. W. Seymour, R. Duncan, J. Strohalm, J. Kopeček, *J. Biomed. Mater. Res.* **1987**, *21*, 1341.
[32] R. Duncan, *Nat. Rev. Cancer* **2006**, *6*, 688.
[33] J. Kopeček, H. Bažilová, *Eur. Polym. J.* **1973**, *9*, 7.
[34] M. Bohdanecky, H. Bažilová, J. Kopeček, *Eur. Polym. J.* **1974**, *10*, 405.
[35] R. Duncan, L. W. Seymour, K. B. O'Hare, P. A. Flanagan, S. Wedge, I. C. Hume, K. Ulbrich, J. Strohalm, V. Subr, F. Spreafico, *J. Controlled Release* **1992**, *19*, 331.
[36] P. A. Vasey, S. B. Kaye, R. Morrison, C. Twelves, P. Wilson, R. Duncan, A. H. Thomson, L. S. Murray, T. E. Hilditch, T. Murray, *Clin. Cancer Res.* **1999**, *5*, 83.
[37] L. W. Seymour, D. R. Ferry, D. Anderson, S. Hesslewood, P. J. Julyan, R. Poyner, J. Doran, A. M. Young, S. Burtles, D. J. Kerr, *J. Clin. Oncol.* **2002**, *20*, 1668.
[38] J. M. Rademaker-Lakhai, C. Terret, S. B. Howell, C. M. Baud, R. F. de Boer, D. Pluim, J. H. Beijnen, J. H. M. Schellens, J.-P. Droz, *Clin. Cancer Res.* **2004**, *10*, 3386.
[39] C. Petr, K. Eva, J. Olga, K. Libor, U. Karel, E. Tomáš, *Macromol. Biosci.* **2015**, *15*, 839.
[40] H. Nakamura, T. Etrych, P. Chytil, M. Ohkubo, J. Fang, K. Ulbrich, H. Maeda, *J. Controlled Release* **2014**, *174*, 81.
[41] M. Šírová, J. Strohalm, P. Chytil, O. Lidický, J. Tomala, B. Říhová, T. Etrych, *J. Controlled Release* **2017**, *246*, 1.
[42] S. Ganta, H. Devalapally, A. Shahiwala, M. Amiji, *J. Controlled Release* **2008**, *126*, 187.
[43] S. Mura, J. Nicolas, P. Couvreur, *Nat. Mater.* **2013**, *12*, 991.
[44] X. Xu, P. E. Saw, W. Tao, Y. Li, X. Ji, S. Bhasin, Y. Liu, D. Ayyash, J. Rasmussen, M. Huo, J. Shi, O. C. Farokhzad, *Adv. Mater.* **2017**, *29*, 1700141.
[45] G. K. Balendiran, R. Dabur, D. Fraser, *Cell Biochem. Funct.* **2004**, *22*, 343.
[46] R. R. Perry, J. A. Mazetta, M. Levin, S. C. Barranco, *Cancer* **1993**, *72*, 783.
[47] Y. Xia, H. He, X. Liu, D. Hu, L. Yin, Y. Lu, W. Xu, *Polym. Chem.* **2016**, *7*, 6330.
[48] C. Wang, L. Liu, H. Cao, W. Zhang, *Biomater. Sci.* **2017**, *5*, 274.
[49] S. Wannasarit, S. Wang, P. Figueiredo, C. Trujillo, F. Eburnea, L. Simón-Gracia, A. Correia, Y. Ding, T. Teesalu, D. Liu, R. Wiwattanapatapee, H. A. Santos, W. Li, *Adv. Funct. Mater.* **2019**, *29*, 1905352.
[50] P. Vaupel, F. Kallinowski, P. Okunieff, *Cancer Res.* **1989**, *49*, 6449.
[51] J. S. Fang, R. D. Gillies, R. A. Gatenby, *Semin. Cancer Biol.* **2008**, *18*, 330.

[52] R. A. Cardone, V. Casavola, S. J. Reshkin, *Nat. Rev. Cancer* **2005**, *5*, 786.
[53] J. Cui, Y. Yan, Y. Wang, F. Caruso, *Adv. Funct. Mater.* **2012**, *22*, 4718.
[54] S. Bertoni, Z. Liu, A. Correia, J. P. Martins, A. Rahikkala, F. Fontana, M. Kemell, D. Liu, B. Albertini, N. Passerini, W. Li, H. A. Santos, *Adv. Funct. Mater.* **2018**, *28*, 1806175.
[55] J. Kopeček, P. Kopečková, T. Minko, Z.-R. Lu, *Eur. J. Pharm. Biopharm.* **2000**, *50*, 61.
[56] R. Duncan, *Nat. Rev. Drug Discovery* **2003**, *2*, 347.
[57] C. W. Scales, Y. A. Vasilieva, A. J. Convertine, A. B. Lowe, C. L. McCormick, *Biomacromolecules* **2005**, *6*, 1846.
[58] P. Chytil, T. Etrych, J. Kříž, V. Šubr, K. Ulbrich, *Eur. J. Pharm. Sci.* **2010**, *41*, 473.
[59] J. A. Alfurhood, H. Sun, P. R. Bachler, B. S. Sumerlin, *Polym. Chem.* **2016**, *7*, 2099.
[60] C. Boyer, M. H. Stenzel, T. P. Davis, *J. Polym. Sci., Part A: Polym. Chem.* **2011**, *49*, 551.
[61] K. J. Thurecht, I. Blakey, H. Peng, O. Squires, S. Hsu, C. Alexander, A. K. Whittaker, *J. Am. Chem. Soc.* **2010**, *132*, 5336.
[62] A. B. Cook, S. Perrier, *Adv. Funct. Mater.* **2020**, *30*, 1901001.
[63] A. K. Pearce, B. E. Rolfe, P. J. Russell, B. W.-C. Tse, A. K. Whittaker, A. V. Fuchs, K. J. Thurecht, *Polym. Chem.* **2014**, *5*, 6932.
[64] Y. Hirai, T. Terashima, M. Takenaka, M. Sawamoto, *Macromolecules* **2016**, *49*, 5084.
[65] V. Taresco, L. Gontrani, F. Crisante, I. Francolini, A. Martinelli, L. D'Ilario, F. Bordi, A. Piozzi, *J. Phys. Chem. B* **2015**, *119*, 8369.
[66] Y. Tominaga, M. Mizuse, A. Hashidzume, Y. Morishima, T. Sato, *J. Phys. Chem. B* **2010**, *114*, 11403.
[67] A. Duro-Castano, R. M. England, D. Razola, E. Romero, M. Oteo-Vives, M. A. Morcillo, M. J. Vicent, *Mol. Pharmaceutics* **2015**, *12*, 3639.
[68] Y. Zhou, W. Huang, J. Liu, X. Zhu, D. Yan, *Adv. Mater.* **2010**, *22*, 4567.
[69] S. Patil, A. Sandberg, E. Heckert, W. Self, S. Seal, *Biomaterials* **2007**, *28*, 4600.
[70] N. Schultz, G. Metreveli, M. Franzreb, F. H. Frimmel, C. Syldatk, *Colloids Surf., B* **2008**, *66*, 39.
[71] F. Alexis, E. Pridgen, L. K. Molnar, O. C. Farokhzad, *Mol. Pharmaceutics* **2008**, *5*, 505.
[72] F. C. Giacomelli, I. C. Riegel, C. L. Petzhold, N. P. Da Silveiras, P. Stěpánek, *Langmuir* **2009**, *25*, 3487.
[73] B. Deng, P. Ma, Y. Xie, *Nanoscale* **2015**, *7*, 12773.
[74] C. Conte, F. Mastrotto, V. Taresco, A. Tchoryk, F. Quaglia, S. Stolnik, C. Alexander, *J. Controlled Release* **2018**, *277*, 126.
[75] T. K. Endres, M. Beck-Broichsitter, O. Samsonova, T. Renette, T. H. Kissel, *Biomaterials* **2011**, *32*, 7721.
[76] Q. Feng, Y. Liu, J. J. Huang, K. Chen, J. J. Huang, K. Xiao, *Sci. Rep.* **2018**, *8*, 2082.
[77] C. Graf, Q. Gao, I. Schütz, C. N. Noufele, W. Ruan, U. Posselt, E. Korotianskiy, D. Nordmeyer, F. Rancan, S. Hadam, A. Vogt, J. Lademann, V. Haucke, E. Rühl, *Langmuir* **2012**, *28*, 7598.
[78] J. Zaias, M. Mineau, C. Cray, D. Yoon, N. H. Altman, *J. Am. Assoc. Lab. Anim. Sci.* **2009**, *48*, 387.
[79] C. Cilliers, I. Nessler, N. Christodolu, G. M. Thurber, *Mol. Pharmaceutics* **2017**, *14*, 1623.
[80] L. Q. Jiang, T. Y. Wang, T. J. Webster, H.-J. Duan, J. Y. Qiu, Z. M. Zhao, X. X. Yin, C. L. Zheng, *Int. J. Nanomed.* **2017**, *12*, 6383.
[81] H. H. Gustafson, D. Holt-Casper, D. W. Grainger, H. Ghandehari, *Nano Today* **2015**, *10*, 487.
[82] B. D. Chithrani, W. C. W. Chan, *Nano Lett.* **2007**, *7*, 1542.
[83] X. Li, *J. Appl. Phys.* **2012**, *111*, 024702.
[84] G. Bao, X. R. Bao, *Proc. Natl. Acad. Sci. USA* **2005**, *102*, 9997.
[85] H. Gao, W. Shi, L. B. Freund, *Natl. Acad. Sci.* **2005**, *102*, 9469.
[86] S. S. Yu, C. M. Lau, S. N. Thomas, W. G. Jerome, D. J. Maron, J. H. Dickerson, J. A. Hubbell, T. D. Giorgio, *Int. J. Nanomed.* **2012**, *7*, 799.
[87] J. V. Frangioni, *Curr. Opin. Chem. Biol.* **2003**, *7*, 626.
[88] J. Yang, K. Luo, H. Pan, P. Kopečková, J. Kopeček, *React. Funct. Polym.* **2011**, *71*, 294.
[89] M. Elsabahy, K. L. Wooley, *Chem. Soc. Rev.* **2012**, *41*, 2545.
[90] H. S. Choi, W. Liu, P. Misra, E. Tanaka, J. P. Zimmer, B. I. Ipe, M. G. Bawendi, J. V. Frangioni, *Nat. Biotechnol.* **2007**, *25*, 1165.
[91] M. R. Dreher, W. Liu, C. R. Michelich, M. W. Dewhirst, F. Yuan, A. Chilkoti, *J. Natl. Cancer Inst.* **2006**, *98*, 335.
[92] D. E. Owens, N. A. Peppas, *Int. J. Pharm.* **2006**, *307*, 93.
[93] J. Liu, F. Zeng, C. Allen, *Eur. J. Pharm. Biopharm.* **2007**, *65*, 309.
[94] R. Kumar, I. Roy, T. Y. Ohulchanskky, L. A. Vathy, E. J. Bergey, M. Sajjad, P. N. Prasad, *ACS Nano* **2010**, *4*, 699.
[95] M. Longmire, P. L. Choyke, H. Kobayashi, *Nanomedicine* **2008**, *3*, 703.
[96] S. S. K. Dasa, R. Suzuki, E. Mugler, L. Chen, R. Jansson-Löfmark, E. Michaëlsson, L. Lindfors, A. L. Klibanov, B. A. French, K. A. Kelly, *Nanomedicine* **2017**, *13*, 2565.
[97] S. AbuHammad, M. Zihlif, *Genomics* **2013**, *101*, 213.
[98] V. Y. Chen, M. M. Posada, L. Zhao, G. R. Rosania, *Pharm. Res.* **2007**, *24*, 2156.
[99] P. D. Roepe, *Biochemistry* **1992**, *31*, 12555.
[100] A. Krarup-Hansen, K. Wassermann, S. N. Rasmussen, M. Dalmark, *Acta Oncol.* **1988**, *27*, 25.
[101] L. Kostka, L. Kotrchová, V. Šubr, A. Libánská, C. A. Ferreira, I. Malátová, H. J. Lee, T. E. Barnhart, J. W. Engle, W. Cai, M. Šírová, T. Etrych, *Biomaterials* **2020**, *235*, 119728.
[102] H. Pan, M. Sima, J. Yang, J. Kopeček, *Macromol. Biosci.* **2013**, *13*, 155.
[103] Y. Yang, D. Pan, K. Luo, L. Li, Z. Gu, *Biomaterials* **2013**, *34*, 8430.
[104] G. Minotti, P. Menna, E. Salvatorelli, G. Cairo, L. Gianni, *Pharmacol. Rev.* **2004**, *56*, 185.
[105] X. Peng, B. Chen, C. C. Lim, D. B. Sawyer, *Mol. Interventions* **2005**, *5*, 163.
[106] Y. Matsumura, T. Hamaguchi, T. Ura, K. Muro, Y. Yamada, Y. Shimada, K. Shirao, T. Okusaka, H. Ueno, M. Ikeda, N. Watanabe, *Br. J. Cancer* **2004**, *91*, 1775.
[107] L. M. Kaminskas, V. M. McLeod, B. D. Kelly, G. Sberna, B. J. Boyd, M. Williamson, D. J. Owen, C. J. H. Porter, *Nanomedicine* **2012**, *8*, 103.
[108] L. M. Kaminskas, V. M. McLeod, B. D. Kelly, C. Cullinane, G. Sberna, M. Williamson, B. J. Boyd, D. J. Owen, C. J. H. Porter, *Mol. Pharmaceutics* **2012**, *9*, 422.
[109] T. Nakanishi, S. Fukushima, K. Okamoto, M. Suzuki, Y. Matsumura, M. Yokoyama, T. Okano, Y. Sakurai, K. Kataoka, *J. Controlled Release* **2001**, *74*, 295.